Transient analysis of solar pyrolysis and hydrogen yield via interband cascade laser absorption spectroscopy of methane, acetylene, ethylene, and ethane

Barathan Jeevaretanam, Mostafa Abuseada, Chuyu Wei, Nicolas Q Minesi, Timothy S Fisher, R. Mitchell Spearrin

Applications in Energy and Combustion Science 16 (2023) 100223

Contents lists available at ScienceDirect

Applications in Energy and Combustion Science

journal homepage: www.elsevier.com/locate/jaecs

Transient analysis of solar pyrolysis and hydrogen yield via interband cascade laser absorption spectroscopy of methane, acetylene, ethylene, and ethane

Barathan Jeevaretanam *, Mostafa Abuseada, Chuyu Wei, Nicolas Q. Minesi, Timothy S. Fisher, R. Mitchell Spearrin

Department of Mechanical and Aerospace Engineering, University of California Los Angeles, Los Angeles, CA 90095, USA

ARTICLE INFO

Keywords:
Hydrocarbon pyrolysis
Laser absorption spectroscopy
Hydrogen
Mid-wave infrared
CH_4 cross-sections

ABSTRACT

A mid-infrared laser absorption sensing method has been developed to measure species concentrations of four hydrocarbons and gas temperature over a range of temperatures in mixture compositions relevant to the pyrolytic decomposition of natural gas. The four measured species (methane, acetylene, ethylene, and ethane) are the most abundant hydrocarbons during the pyrolysis of natural gas, and provide a means to monitor decomposition progress and hydrogen yield through molar balance. In this work, time-division multiplexed signals of three distributed-feedback interband cascade lasers are used to make simultaneous measurements of select C-H stretch rovibrational transitions of the target hydrocarbons in the 3.00–3.34 μm range. The sensor was validated over a range of temperatures and pressures (300–1000 K, 0.03–1 atm) at relevant mixture compositions, with correction methods developed to mitigate cross-species interference. The sensor was demonstrated on a solar-thermal pyrolysis reactor, where time-resolved measurements of species mole fractions were performed across a range of insolation conditions to capture the transient response of the reactor.

1. Introduction

Hydrogen (H_2) is considered to be an important alternative to traditional hydrocarbon fuels for the purpose of decreasing global anthropogenic carbon dioxide (CO_2) emissions [1]. Currently, approximately 96% of H_2 is produced via thermochemical conversion of carbon-based fuels [2]. Of these thermochemical processes, the leading method for hydrogen production is steam-methane reforming (SMR) [3]. In this endothermic reaction, high temperature steam reacts with methane (CH_4) gas to produce H_2 amongst byproducts that include CO_2. The heat source for this reaction is primarily derived from the use of fossil fuels, further increasing the net CO_2 emissions [4]. CH_4 pyrolysis offers an alternative to SMR for hydrogen production with less CO_2 emissions [5]. The global chemical equation for this reaction is given by:

$$CH_4 \rightarrow C + 2H_2 \tag{1}$$

Like SMR, the pyrolysis of CH_4 is also an endothermic reaction. However, the absence of any oxidizer in the reactants precludes the formation of CO_2 in the products. In addition, the pure solid carbon products formed through the pyrolytic reaction are more readily separated from the gaseous product stream and sold or stored at a favorable economical value compared to gaseous oxidized carbon [6]. Here, we report detailed optical diagnostics of the gaseous product stream in a methane pyrolysis reaction driven by solar-thermal stimulus.

As shown below, the pyrolytic decomposition of CH_4 generally progresses in a stepwise dehydrogenation, where the successive loss of H_2 molecules corresponds with the formation of stable intermediates with increased C:H ratio [7].

$$2CH_4 \xrightarrow{-H_2} C_2H_6 \xrightarrow{-H_2} C_2H_4 \xrightarrow{-H_2} C_2H_2 \xrightarrow{-H_2} 2C \tag{2}$$

The CH_4 decomposition process is simulated using a more comprehensive reaction mechanism (USC Mech II) at a constant temperature of 1400 K in Fig. 1, showing that methane, acetylene (C_2H_2), ethylene (C_2H_4), and ethane (C_2H_6) represent the dominant gas-phase intermediate and product constituents [8]. As such, quantitative measurements of these four hydrocarbons in the product stream provide critical information about reaction progress as well as process efficiency. Although the present work focuses on methane pyrolysis, it is important to note that other, larger hydrocarbon feedstocks (alkane, alkene,

* Corresponding author.
E-mail address: barathan@ucla.edu (B. Jeevaretanam).

https://doi.org/10.1016/j.jaecs.2023.100223
Received 12 September 2023; Received in revised form 30 October 2023; Accepted 9 November 2023
Available online 10 November 2023

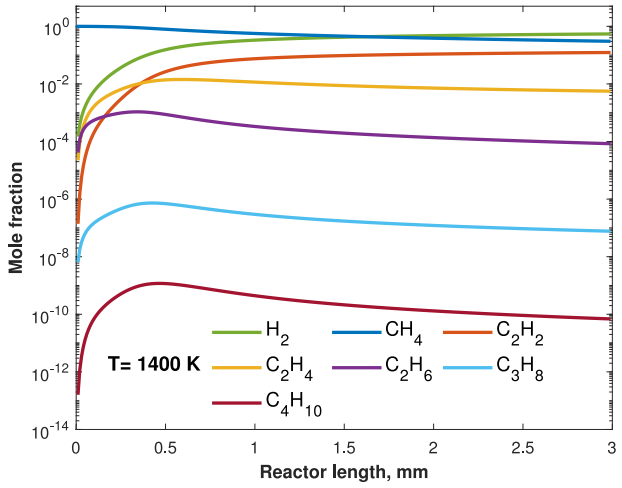

Fig. 1. Species evolutions obtained from a chemical kinetic simulation of CH_4 decomposition through a plug flow reactor at 25 torr and a gas flow rate of 100 sccm using CANTERA [22]. Relevant reactions were obtained from the USC Mech II chemical mechanism [8].

and alkyne) similarly decompose into these intermediates which represent the smallest stable species of various carbon-hydrogen bond structures [9].

This work focuses on CH_4 pyrolysis due to the abundance of CH_4 in natural gas, the most common feedstock in H_2 production. In this context, it can be shown that measurement of the target hydrocarbon species can well-characterize the gas-phase output with hydrogen being the only remaining species of significant concentration. Time-resolved species measurements may further be used in process development or control, where a snapshot of reaction progress or process efficacy can then inform changes to operational parameters to improve yield quality.

CH_4 pyrolysis has been studied through a multitude of reactor configurations (fixed bed, fluidized bed, plasma-assisted) and through catalyzed or uncatalyzed processes [10–12]. Typically, the product stream for such systems is characterized ex-situ via either mass spectrometry (MS) or gas chromatography (GC). The inherent response times of these sample-based monitoring techniques (on the order of seconds to minutes) are often adequate for final product compositional analysis. However, in order to elucidate transient decomposition behavior and to optimize process conditions in real time, particularly under variable heating, faster response times are desired. In addition, the quantification of trace species such as C_2H_4 and C_2H_6 requires high sensitivity, often outside the detection range of more portable and affordable MS and GC devices [13]. GC-MS also typically requires calibration to be quantitative, which can be challenging in complex gas mixtures.

By contrast, laser absorption spectroscopy (LAS) provides a highly quantitative, calibration-free, and in-situ or in-stream method for measuring both dominant and trace hydrocarbon species formed in the pyrolytic decomposition of CH_4 based on molecular structure rather than mass or chemical interactions. LAS sensing of CH_4, C_2H_2, C_2H_4, and C_2H_6 has been demonstrated across a variety of applications. These applications include environmental monitoring [14,15], combustion chemistry studies [16–18] and planetary sciences [19] as well. The recent emergence of distributed-feedback interband cascade lasers (DFB-ICLs) has enabled highly sensitive detection of these C1-C2 hydrocarbons in the C-H stretch fundamental bands [20,21], providing enhanced detection limits and in situ measurements over short optical pathlengths.

In a recent study by our research group, Wei et al. [23] employed an LAS measurement technique to characterize the product stream in a solar-thermal pyrolysis reactor. In that work, two DFB-ICLs were deployed to measure CH_4, C_2H_4, and C_2H_6 at the exhaust of a solar reactor through regularly-intervaled diversion of the beams on the order of Hz. The method was used to make species measurements over a range of pyrolysis conditions, and provided important benchmark data for comparison to first-order chemical kinetic models of the reactor [23].

The present work advances upon this prior LAS sensor development via several key elements: (1) addition and integration of a C_2H_2 measurement strategy to further understanding of the latter dehydrogenation steps and to improve estimation of hydrogen yield, (2) simultaneous kHz-rate sensing of the four hydrocarbon species via time-division-multiplexing on a shared beam path, and (3) extension of the thermodynamic range of the multi-species LAS method to elevated temperatures with validated correction methods to mitigate the effects of cross-species interference. In this paper, we present the theory and methods underlying this novel laser diagnostic strategy for time-resolved measurement of species yields in hydrocarbon pyrolysis. Sensor capabilities are tested via a series of validation tests and a demonstration for transient analysis of a solar-thermal pyrolysis reactor.

2. Laser absorption spectroscopy (LAS)

2.1. Theory

The theory of LAS is extensively outlined in prior work [24] and is only briefly discussed here to clarify nomenclature. Thermodynamic gas properties and species mole fraction, X_{abs}, are related to the transmitted intensity of monochromatic light by the Beer–Lambert law given by:

$$\begin{aligned}\alpha_v &= -\ln\left(\frac{I_t}{I_0}\right)_v \\ &= \sum_i P x_{\text{abs}} S_i(T) \varphi_i\left(v, T, P, X_{\text{abs}}\right) L\end{aligned} \tag{3}$$

where I_t/I_o is the ratio of experimentally measured transmitted and incident laser intensity at frequency v [cm^{-1}], α_v is the spectral absorbance at that frequency, P [atm] is the total pressure, $S_i(T)$[cm^{-2}/atm] is the temperature-dependent linestrength of transition i at temperature T [K], L [cm] is the pathlength of the absorbing medium, and φ_i [cm] is the spectral lineshape of transition i. Integrating over the spectral domain of a well-isolated transition yields the absorbance area, A_i:

$$A_i = \int_{-\infty}^{\infty} \alpha_v dv = P S_i(T) x_{\text{abs}} L \tag{4}$$

This integration eliminates the lineshape dependence on the absorbance area. In practice, this is achieved by fitting an assumed lineshape to the measured spectra. With independent knowledge of pressure, temperature, and the pathlength of the absorbing gas, the species mole fraction may be determined.

In addition, the availability of two sufficiently-isolated transitions of a given species allows for a gas temperature measurement through a two-line thermometry technique. By taking a ratio of the absorbance areas of these transitions, the dependence on pressure, species mole fraction, and pathlength is eliminated. As a result, the ratio of areas shown in Eq. (5) is only dependent on temperature, as below:

$$\frac{A_i}{A_j} = \frac{S_i(T)}{S_j(T)} \tag{5}$$

Eq. (5) can then be solved to obtain the temperature of a given gas.

2.2. Wavelength selection

Recent advances in laser technology have made the strongest mid-wave infrared (IR) vibrational bands of hydrocarbons readily-accessible for tunable laser absorption spectroscopy. The line survey in Fig. 2 shows several vibrational bands of the target hydrocarbons (methane, acetylene, ethylene, and ethane) in the infrared, including the fundamental C-H stretch vibrational bands in mid-IR (3–4 μm). These fundamental bands are orders of magnitude stronger than the overtone and combination bands found in the near-IR. In this work, interband cascade lasers are used to probe these strong mid-IR transitions, and facilitate sensitive measurement of hydrocarbons formed in pyrolytic reactions.

Select rovibrational transitions from the C-H stretch bands in the 3.00–3.34 μm range (indicated by the dashed lines in the line survey and the absorbance subplot in Fig. 2) were chosen to probe each hydrocarbon. The R(15) manifold of the ν_3 band of CH_4 was selected for measurements near room temperature due to its relative strength and isolation from other hydrocarbon transitions [25]. The strong absorption linestrength enables a wide dynamic range of X_{CH_4} measurements, a critical requirement for characterizing the efficacy of pyrolytic reactors that use either CH_4 or natural gas as a feed gas. However, at elevated temperatures ($T > 479$ K), this R(15) manifold can become optically thick at moderate pathlengths (~10 cm), thus preventing accurate inference of X_{CH_4}. To avert this issue and extend the range of operation, a separate wavelength region consisting of multiple transitions adjacent to the R(15) manifold was instead used for X_{CH_4} determination. These two separate wavelength regions are shown in the middle inset of the spectral simulation subplot in Fig. 2, also highlighting the R(14) transition of the ν_9 band of C_2H_4 that was probed in this work. This C_2H_4 transition was selected primarily for its proximity to the R(15) manifold of CH_4 [23], enabling simultaneous measurement of the two species using one laser. Acetylene is commonly the second most abundant product species during the pyrolysis of CH_4 or natural gas, and was probed here by measurement of the adjacent R(24) and R(18) line pair of the $\nu_2 + \nu_4 + \nu_5$ and ν_3 bands, respectively [26]. These transitions were selected for their strong absorption linestrengths and relative isolation from the transitions of other hydrocarbons, enabling determination of $X_{C_2H_2}$ without any necessary interference-mitigating correction methods. The trace amount of C_2H_6 formed in the aforementioned pyrolytic reactions was measured by targeting the intense $^RQ_3$ line cluster near 2996.86 cm^{-1}, selected for strength and relative isolation [27]. The management of cross-species interference at this wavelength at certain conditions is further detailed in the sensor validation and data processing section.

2.3. Optical setup

Three distributed feedback interband cascade lasers were used in this work to target the four hydrocarbons in a time-division-multiplexed optical configuration (see Fig. 3). Colinear propagation and delivery of the three beams from the breadboard were achieved using two carefully-aligned CaF_2 beam splitters. Time-multiplexed trapezoidal waveforms of varying effective duty cycle (20%–30%) was selected for modulation as it maximized the output laser beam power during the scan period while minimizing any ringing effects and also allowing all three lasers to scan during a single period, providing a raw measurement rate of 10 kHz [31]. The colinear, time-multiplexed laser beams were transmitted through sapphire windows and focused onto a single photovoltaic (PV) detector (VIGO System PVI-4TE-5, 100 MHz bandwidth). A 2-inch germanium etalon with a free spectral range of 0.024 cm^{-1} was placed along the beam path to convert light intensity signals from the time domain to the wavenumber domain. These etalon signals were recorded for each laser prior to each test. All signals were recorded using a 200-MHz bandwidth oscilloscope (Picoscope 5000 series). A raw sample signal of the simultaneous measurement of the spectra of the four hydrocarbons is shown in Fig. 4. A phase-locked average was often employed to improve signal to noise ratio (SNR) and detection at trace levels and yielded an effective time resolution of 1 ms, more than adequate for process monitoring. In addition to facilitating the simultaneous measurement of the hydrocarbon species, this optical configuration and time-multiplexing scheme removed the need for active physical diversion of the individual beams through the use of a flip mirror as employed by Wei et al. [23], which had been cumbersome and significantly limited overall measurement rate. This compact, modular configuration allowed for the seamless integration of the LAS sensor module with both the solar-thermal reactor and the high-temperature gas cell that was used for validation measurements.

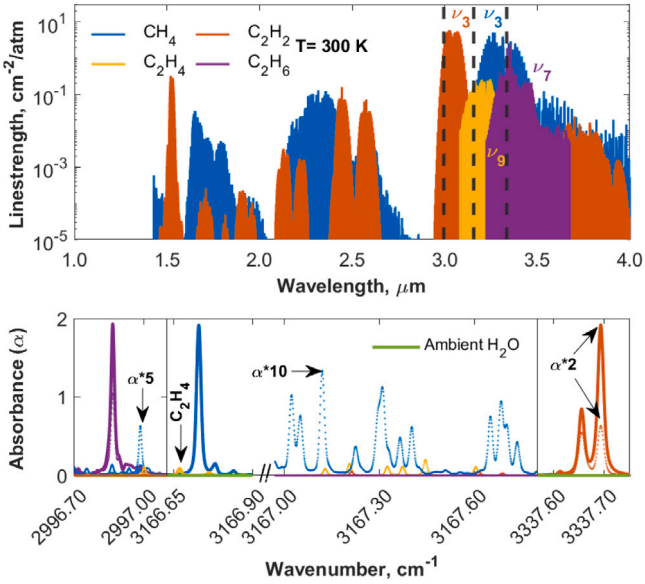

Fig. 2. (Top) Absorption linestrengths of hydrocarbons relevant to this study computed from the HITEMP [28] database (CH_4), HITRAN [29] database (C_2H_2 and C_2H_4) and cross-sectional database by Harrison et al. [30] (C_2H_6). Dashed lines indicate the specific wavelengths used. (Bottom) Spectral simulations of the measured transitions and interfering partners at $P = 45$ torr, $L = 10$ cm, and mole fractions: 92% CH_4, 4% C_2H_2, 3% C_2H_4 and 1% C_2H_6 at $T = 300$ K (solid lines) and at $T = 600$ K (dashed lines). Simulations of H_2O are included to account for potential ambient absorption in the beam path of the lasers.

3. Sensor validation

In this section, the species-specific spectroscopic methods employed to make quantitative inferences of individual species mole fractions are detailed. For these validation measurements, the LAS sensor module described in the previous section was aligned on an optically-accessible heated gas cell [32] as illustrated in Fig. 3. Measurements presented in this section were made using a gas mixture with the following nominal composition: 92.05% CH_4, 4% C_2H_2, 3% C_2H_4, and 0.95% C_2H_6. This specific composition was selected to enable the investigation of spectral interference and demonstrate the sensor capability to perform species measurements at a relevant composition to the pyrolysis of natural gas and methane, which is the primary target application.

3.1. Data processing & fitting procedures

Measured absorbance spectra were least-squares fitted with Voigt lineshapes, and quantitative inference of species abundance was achieved using spectral parameters from HITEMP (CH_4), HITRAN (C_2H_2 and C_2H_4) and the cross-sectional database by Harrison et al. (C_2H_6). The Doppler linewidth for all lines was calculated using an average temperature measured from three thermocouples equally spaced along the length of the gas cell. The static pressure of the gas was measured using capacitance manometers.

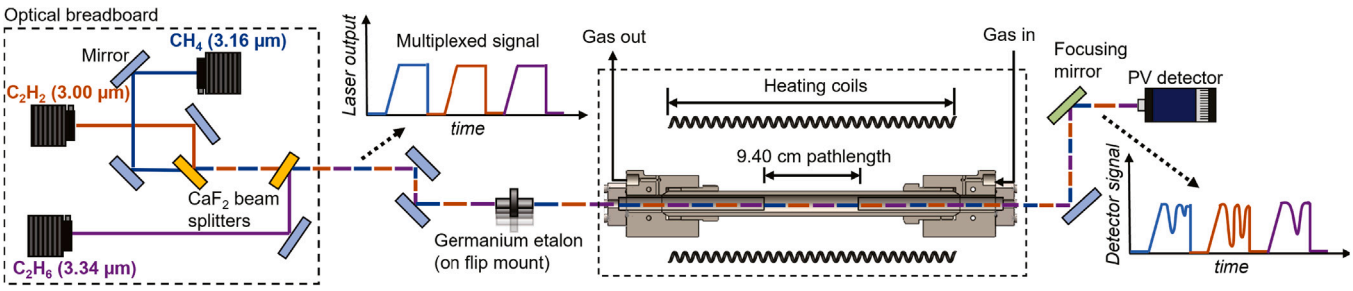

Fig. 3. Schematic illustrating the LAS sensor module (left) interfaced with the high-temperature gas cell (right).

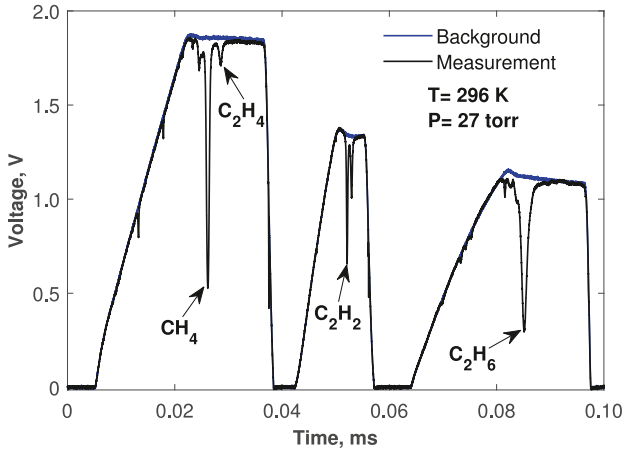

Fig. 4. Time-division multiplexed raw signals illustrating the simultaneous measurement of the spectra of all four hydrocarbons in a gas cell with an optical pathlength of 9.4 cm. The species mole fractions are: 92.05% CH_4, 4% C_2H_2, 3% C_2H_4 and 0.95% C_2H_6.

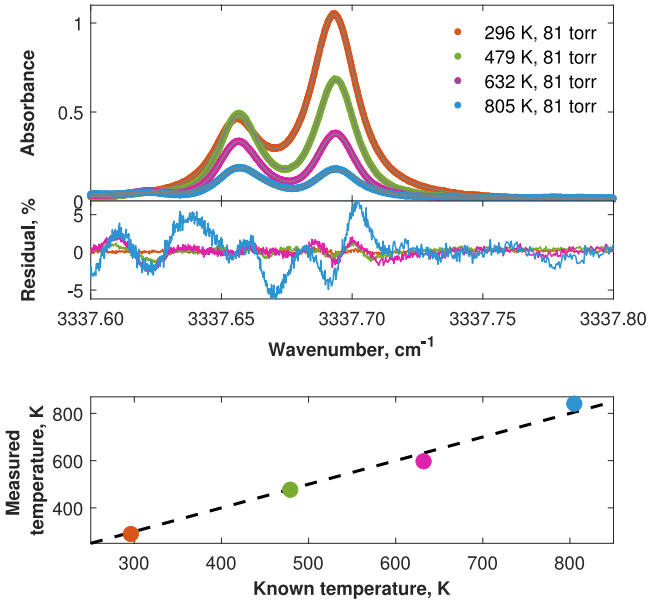

Fig. 5. (Top) Measured C_2H_2 spectra at a range of temperatures with spectral fits and accompanying residuals, each normalized by the respective spectrum's peak absorbance value. (Bottom) Measured temperatures obtained from the two-line thermometry technique.

3.1.1. C_2H_2 spectral fitting and thermometry

The spectral region at which the C_2H_2 measurement was made is free of interference from other measured hydrocarbons. This allows for direct spectral fitting of the measurement without need for interference-correction. The two C_2H_2 transitions were least-squares fitted using Voigt profiles with the absorbance areas, A_i and collisional linewidths, ν_c treated as free parameters directly. The mole fraction, $X_{C_2H_2}$, was then recovered from both these fitted absorbance areas through the application of Eq. (4). The availability of two closely-spaced transitions in the C_2H_2 measurement domain with differing lower state energy enabled the ratiometric inference of the gas temperature as well. Using the measured absorbance area of each transition to obtain an area ratio, Eq. (5) was solved iteratively to obtain temperature. As shown in Fig. 5, this temperature measurement technique demonstrated good accuracy up to ~800 K, with a standard deviation of ~3% from known thermocouple measurements. At temperatures higher than 805 K, the inferred temperature showed significant deviation from thermocouple measurements. This is attributed to the inability of the HITRAN database to fully capture the spectra at these high temperatures (due to additional high rotational energy lines not in HITRAN becoming active) and the relatively low lower-state energy difference of the line pair of 303 cm^{-1}.

3.1.2. Sequential fitting of CH_4 and C_2H_4 spectra

Due to the large disparity in the respective peak absorbance of the target C_2H_4 and CH_4 transitions highlighted in Fig. 6, a simultaneous fit of the two transitions yielded unreliable results, with the fitting routine exhibiting a bias towards the much stronger CH_4 transition. To address this issue, a sequential fitting routine of the two species' transitions was employed as it yielded more accurate determination of $X_{C_2H_4}$ [33]. Prior to performing a least squares fit of the CH_4 absorbance spectrum, the R(9,14) C_2H_4 transition that is in close proximity to the R(3,15) manifold of CH_4 was omitted from the spectral region of interest. The isolated CH_4 transition was then fitted using X_{CH_4} and ϕ as free parameters. ϕ is defined as a scale factor to the air-broadening coefficient, $\gamma_{abs,air}$, in the collisional linewidth of the transition given by:

$$\Delta\nu_c = 2P_{\text{tot}}[X_{abs}\gamma_{abs,\text{self}}(T) + \phi(1 - X_{abs})\gamma_{abs,\text{air}}(T)] \quad (6)$$

Here, P_{tot} is the total pressure of the gas mixture and $\gamma_{abs,self}$ is the temperature-depenedent self-broadening coefficient. $\gamma_{abs,air}$ is scaled in this manner in the fitting procedure to account for the absence of broadening coefficient data of the colliding partners in the gas mixture.

To fit the C_2H_4 absorbance spectrum, only CH_4 transitions in the measurement were first fitted as described above. The fitted CH_4 spectrum was then subtracted from the measurement to yield a residual spectrum that consisted only of the contributions from C_2H_4 as shown in the middle subplot of Fig. 6. This residual spectrum was then least-squares fitted with a Voigt profile with $X_{C_2H_4}$ and ϕ treated as free parameters.

To reconcile the optically thick R(15) CH_4 manifold at elevated temperatures ($T > 500$ K), a separate region of the spectral scan was used to perform a broadband spectral fit (3167.2 cm^{-1}–3167.9 cm^{-1}) of multiple methane transitions. In this spectral region, interference

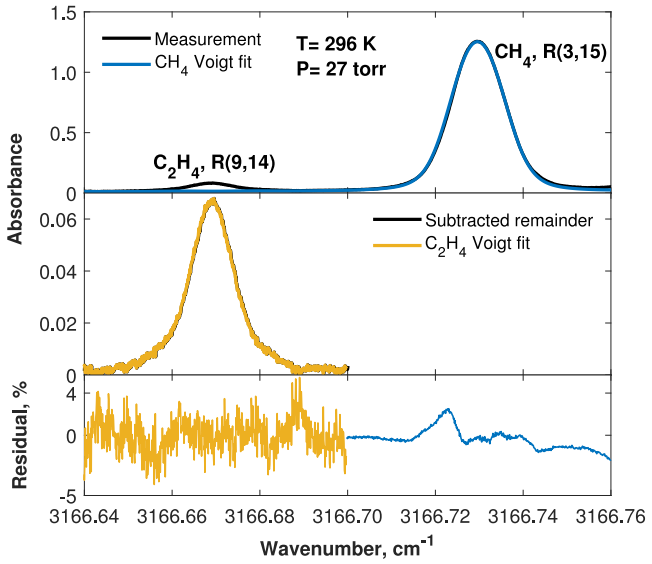

Fig. 6. (Top) Measurement containing both CH_4 and C_2H_4 transitions with a CH_4 Voigt fit of the spectral region. (Middle) Leftover spectra obtained upon subtraction of the CH_4 Voigt fit from the measurement. (Bottom) The residuals of the Voigt fits of both species' transitions, normalized by their respective peak absorbance values.

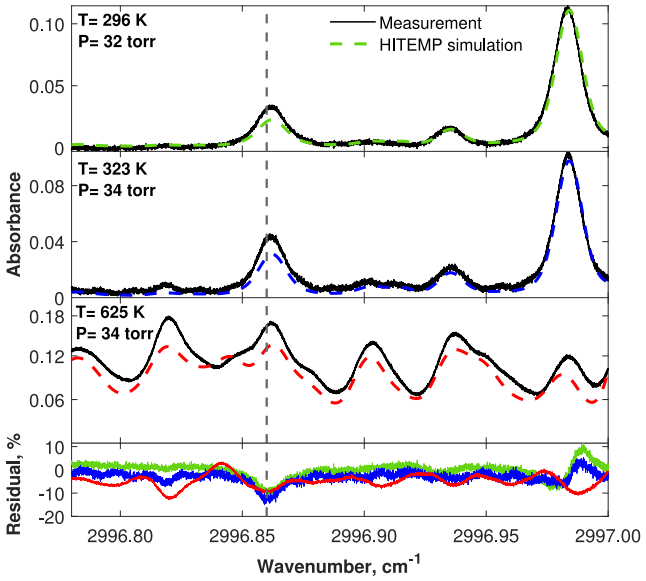

Fig. 7. (Top) Measured pure CH_4 spectra and HITEMP simulations across a range of temperatures. Dashed lines indicate the linecenter of the target C_2H_6 transition. (Bottom) Residuals of the measurement and simulation, normalized by the peak absorbance value of each measured spectrum.

from the other three hydrocarbons in the gas mixture was negligible in magnitude. As before, the free parameters for this least-squares fit were X_{CH_4} and ϕ.

3.1.3. CH_4 interference mitigation for C_2H_6 sensing

Accurate determination of $X_{C_2H_6}$ required implementation of a correction method to account for the contribution of broadband CH_4 interference in the vicinity of the target C_2H_6 transitions. Initially, a sequential approach, similar to that used for the determination of $X_{C_2H_4}$, was employed. The broadband contribution of CH_4 was removed by subtracting a simulated spectrum from the measurement. This simulation was performed using results (X_{CH_4} and ϕ) obtained from the least squares fit of the measured CH_4 spectrum near the 3166 cm^{-1} region and spectral parameters from HITEMP. The spectrum obtained after this subtraction was then least squares fitted similarly with $X_{C_2H_6}$ and ϕ as free parameters. However, this method produced erroneous results, with disagreements of up to 25% in inferred $X_{C_2H_6}$ at elevated temperatures.

Further investigation revealed that spectral simulations using the HITEMP database for CH_4 exhibited considerable disagreement between the measured peak absorbance of select features and the simulation. This discrepancy is highlighted in Fig. 7, where measurements of pure CH_4 were made at 3 different temperatures and compared to HITEMP simulations.

Notably, the discrepancy in absorbance between the methane measurement and the HITEMP simulation in the region near the line cluster of C_2H_6 (~2996.85 cm^{-1}) is significant (as high as 10% at T = 632 K). Therefore, in this spectral region, a spectral simulation using the HITEMP database proved inadequate to remove the broadband CH_4 interference. To accurately capture the broadband CH_4 contribution at this wavelength, absorption cross-sections of pure CH_4 spectra at 2996.7 cm^{-1}–2997.5 cm^{-1} were measured for a range of relevant temperatures and pressures and used to correct the spectral absorption of the multi-species mixtures. The methane cross-section database is included in the supplementary material of this work.

Prior to subtraction from the convoluted measurement, the pure CH_4 spectrum from the database was scaled by the measured mole fraction of CH_4 in the test gas. An example of this scaled spectrum overlaid on the convoluted measurement prior to subtraction is shown in the first subplot of Fig. 8. A least squares fit of this remainder spectrum yielded accurate results of $X_{C_2H_6}$ across a range of temperatures and pressures, with measured mole fraction deviation within 5%.

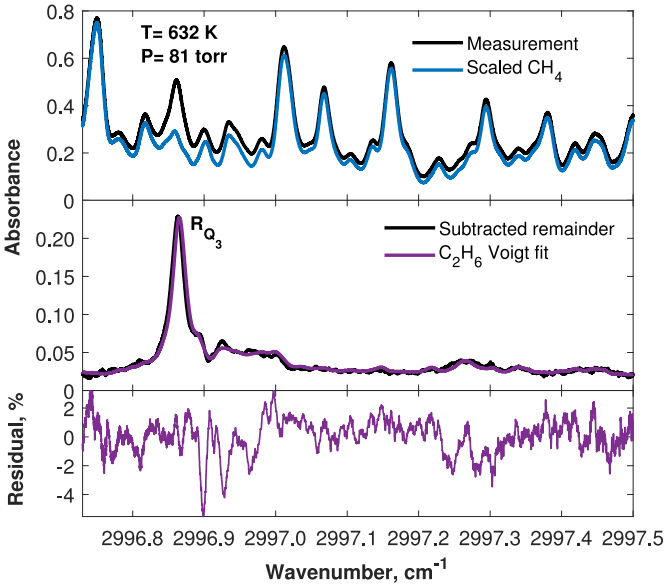

Fig. 8. (Top) Convoluted measurement containing C_2H_6 and CH_4 contributions overlaid with a scaled pure CH_4 spectrum. (Middle) Leftover spectrum obtained upon subtraction of the scaled pure CH_4 spectrum from the measurement. (Bottom) Residual of the Voigt fit of the C_2H_6 spectrum, normalized by the peak absorbance value of the transitions.

3.2. Sensor operating range

As mentioned previously, a gas mixture consisting of the four target hydrocarbon species was used to validate the thermodynamic range and establish detectability limits of the sensor. Fig. 9 shows spectra of all four hydrocarbon species over a representative range of thermodynamic conditions. Room temperature spectra of the species on the top

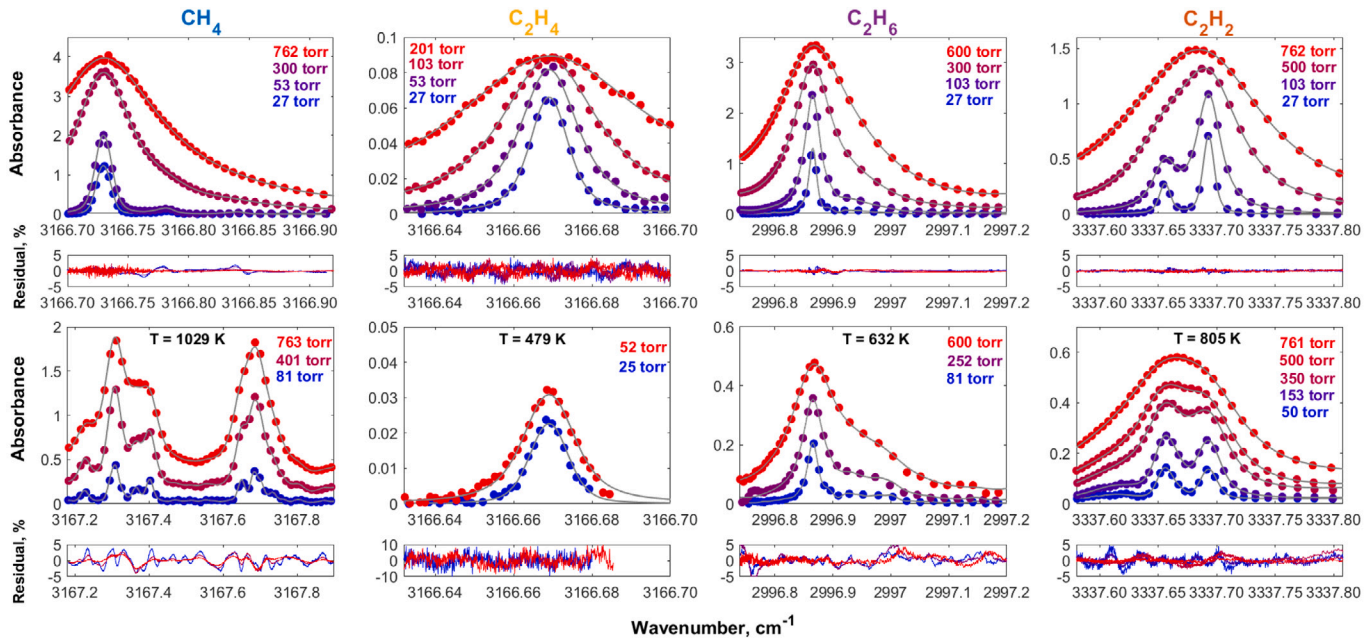

Fig. 9. (L-R) Measured spectra with Voigt fits and accompanying residuals of CH_4, C_2H_4, C_2H_6, and C_2H_2 at $T = 296$ K (top) and elevated temperatures (bottom) across a range of pressures. Note that the spectral range for CH_4 is different at 296 K and 1029 K.

row of this figure are combined with respective high-temperature spectra on the bottom. A requisite validation accuracy of 5% in the species mole fraction measurements was imposed to estimate the range of the sensor with respect to temperature and pressure for each species. This threshold was increased to 8% for C_2H_4 due to its much weaker absorption feature compared to the other hydrocarbons of interest. For CH_4, the spectra were validated up to a maximum temperature of 1029 K through a combination of the two different measurement wavelengths, both shown in Fig. 9. The upper limit of the C_2H_4 measurements ($P =$ 201 torr at $T = 296$ K and $P = 52$ torr at $T = 479$ K) was constrained by: (1) the blending of the weaker C_2H_4 transition with the much stronger CH_4 transition at higher pressures and, (2) the progression of the C_2H_4 transition into the optically thin regime at higher temperatures. As such, its utility is somewhat constrained to low-pressure applications (including the target solar reactor in this work). The C_2H_6 spectra were deconvolved and validated successfully up to approximately 630 K. At higher temperatures, deconvolution of the spectra proved to be more challenging due to the compounding effects of weakening C_2H_6 transitions and strengthening CH_4 transitions with increasing temperature. Coupled with the lack of high-energy transitions in the C_2H_6 cross-section database by Harrison et al., inference of $X_{C_2H_6}$ yielded errors near 20% at the next temperature increment (~800 K). Finally, the C_2H_2 spectra consisting of the two target transitions were validated up to 805 K (50–760 torr). At higher temperatures, the accuracy of the $X_{C_2H_2}$ measurement diminished. Similarly, the line-by-line database of HITRAN failed to accurately capture the C_2H_2 spectra at higher temperatures, likely from a lack of high-energy transitions. Expanding this line-by-line database or building a high-temperature cross-section database would extend the operating range of the current sensor as good SNR remained at such conditions, but such efforts were beyond the scope of this work.

4. Sensor demonstration

In this section, the sensor is demonstrated for time-resolved simultaneous measurements of all four hydrocarbon species on a solar-thermal pyrolysis reactor at a range of experimentally-simulated insolation conditions.

4.1. Experimental setup

The concentrated solar-thermal pyrolysis reactor used in this study is illustrated in Fig. 10. The reactor's hardware and method of operation have been extensively outlined in previous work [23,34], and thus only key elements are included in this work for brevity. In this reactor, concentrated light from a variable output 10 kW_e xenon lamp that mimics the solar spectrum irradiates a thin porous carbon substrate up to temperatures of 1600 K [35]. An IR camera positioned aft of the reaction zone is used to provide a spatially-resolved temperature measurement of the substrate's rear surface. The concentration of light gives rise to a heat-flux distribution closely described by a Lorentzian distribution, where temperature is highest at the center and lowest at the periphery of the substrate [36]. CH_4 gas (99.999%) is flowed into the reactor chamber and through the 3.2-mm thick porous substrate at known flow rates using a mass flow controller (MKS Instruments), initiating decomposition of the inlet gas. The products of this decomposition reaction, consisting mainly of H_2, CH_4, and minor hydrocarbons are expelled through an exhaust line with optical access situated at a vertical distance of 0.29 m from the reaction zone. The LAS sensor module is deployed at this measurement location to characterize the product stream that has cooled to near room temperature, as measured by a thermocouple and confirmed by the acetylene sensor at that location.

For the purpose of this demonstration, the start-up transient response of the reactor is studied at a range of lamp output powers. Leveraging the variable power output of the lamp, the intensity of irradiation incident on the substrate is modulated, effectively controlling the temperature of the reaction zone. The power output of the lamp for these experiments ranged from 0.92 to 2.34 kW while the volumetric flow rate of the CH_4 feed gas and pressure of the reactor are kept constant at 100 sccm and 25 torr, respectively. At each output power condition, the lamp power output is allowed to reach steady state over the course of several minutes. During this period, the substrate is blocked from the lamp's concentrated light by a motorized douser to prevent any fluctuations in the output of the lamp from influencing the decomposition process. Once steady state output of the lamp is established, CH_4 flow into the reaction zone is initiated and the motorized douser is opened, thus commencing the heating of the substrate and decomposition reaction.

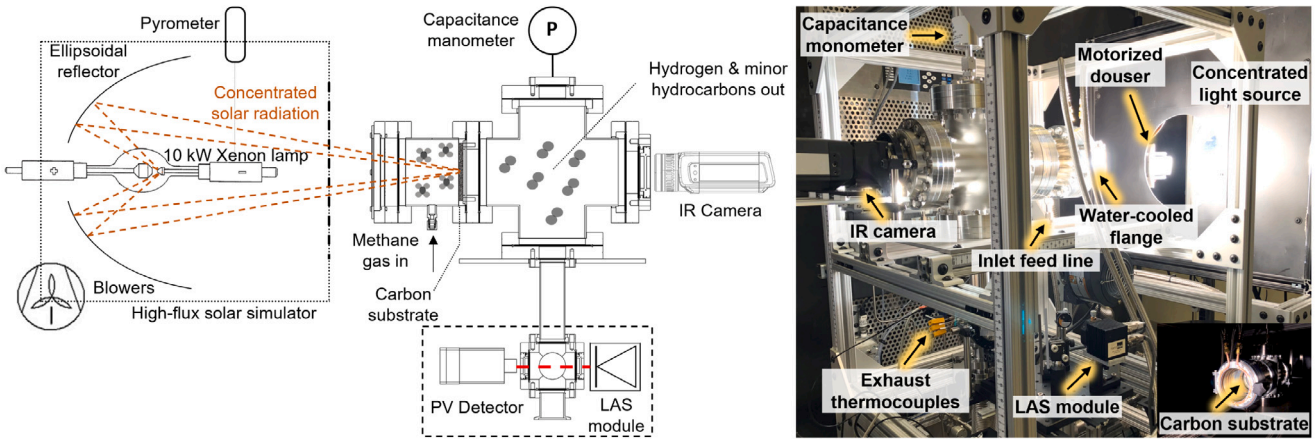

Fig. 10. (Left) Schematic of the solar-thermal pyrolysis reactor with the LAS sensor module located at the exhaust of the reactor. (Right) A photograph of the reactor during operation.

4.2. Results and discussion

The time-division-multiplexed colinear delivery of the three beams at the reactor exhaust facilitated time-resolved simultaneous measurements of all four hydrocarbon species during the decomposition of CH_4, as shown in Fig. 11. Knowledge of these four hydrocarbon species mole fractions provides an indirect measurement of the H_2 mole fraction at any given time by invoking the major products assumption to formulate the equation given below:

$$X_{H_2} = 1 - (X_{CH_4} + X_{C_2H_6} + X_{C_2H_4} + X_{C_2H_2}) \quad (7)$$

Implicit in Eq. (7) is that any minor product excluded in the accounting of the gaseous species forms only in negligible quantities. This is corroborated through supporting mass spectrometry measurements on the reactor [23]. While not tested here, it is notable that the major products assumption is also expected to remain valid for applications with natural gas mixtures that consist primarily of CH_4 and other larger hydrocarbons common to natural gas. During pyrolysis, these larger hydrocarbons (such as ethane, propane, and butane) are expected to similarly decompose into the target C1-C2 intermediates and follow the dehydrogenation pathway of CH_4 as in Eq. (2). However, application of this method with feedstocks that contain appreciable quantities of non-hydrocarbon species such as CO_2 and N_2 which are also common constituents in natural gas, will require modification of Eq. (7) based on a known initial concentration of these inert species. The inclusion of a C_2H_2 measurement, a key product in the decomposition of CH_4, significantly improves and simplifies H_2 yield determination compared to our previous work [23]. Without this measurement, several additional analytical steps such as hydrogen and carbon atom balancing must be first implemented to determine $X_{C_2H_2}$ before application of Eq. (7) is possible [23]. To account for the carbon atoms in particular, physical measurement of the mass of deposited carbon on the substrate surface at the end of each experiment was required, which prevented a time-resolved measurement of hydrogen yield, as is demonstrated here. As such, the present work enables the direct application of Eq. (7) at every measurement interval throughout the duration of the experiment and, importantly, provides a transient quantification of the X_{H_2} yield. The evolution of X_{H_2} is shown in Fig. 11.

Across all species measurements, an apparent lag is observed between the time at which the motorized douser is opened and the detection of the initiation of the decomposition process. This time lag can be attributed to: (1) the transit time of the product gas from the reaction zone to the LAS measurement location and (2) the thermal ramp up of the reaction zone from room temperature due to the irradiation of the concentrated light on the substrate surface. The transit time of the product gas contributes to approximately 3 s of this observed latency as demonstrated in calculations provided in Appendix A. Based on the mass (~4 g), heat capacity, and absorptivity of the carbon substrate, a thermal ramp up period on the order of seconds is expected from direct irradiation. This contrasts volumetric reactors with indirect heating which can require up to hours to achieve steady-state conditions [37]. The rapid heating timescales of this reactor are observed in the experimental data, through both the thermal imaging of the substrate's rear surface and the accompanying time-resolved speciation of the products shown in Fig. 11. The time at which decomposition initiates across all lamp output power conditions shows a strong correlation with this ramp up period, with decomposition beginning only after the substrate surface temperature passes ~1000 K, reflective of the highly temperature-dependent reaction kinetics.

The rate of CH_4 decomposition demonstrates a strong correlation with lamp output power which directly influences substrate temperature. To quantify this effect, the time taken for X_{CH_4} to reach 1/e (~63%) of its equilibrium change in magnitude from the point at which the concentrated light was introduced in the chamber was studied across all lamp output powers. At the extrema of the lamp's output power, this time was measured to be approximately 50 s at 0.92 kW and 10 s at 2.34 kW, accounting for the transit time of the gas from the reaction zone. As expected, the higher reaction zone temperatures associated with higher lamp output powers facilitate more rapid decomposition of the inlet CH_4 stream, resulting in a five-fold increase in decomposition rate at the extremes. This effect may be attributed to the exponential Arrhenius-like temperature dependence in the chemical timescale associated with the cracking of the CH_4 molecules at higher temperatures [38].

The strong dependence of this process on temperature (or lamp output power) is also captured in the steady-state compositions of the product stream across multiple experiments. An increase in the output power from 0.92 kW to 2.34 kW, corresponding to an increase in steady-state peak temperature of approximately 250 K on the substrate surface, substantially altered the composition of the product stream. Across this output power range, the steady-state CH_4 composition for example, fell from 58% to 11%, representing a significant increase in methane conversion. Analogous trends are observed across the other measured hydrocarbons, excluding C_2H_2. The steady-state C_2H_2 composition in the product stream is minimally affected by changes in output power of the lamp, with mole fractions only varying within 15% of the measured maximum.

The steady-state composition of the product stream further indicates an incomplete decomposition process. For example, decomposition at the highest lamp output power resulted in a measured steady-state product composition of approximately 85% H_2, 11% CH_4, 2.9% C_2H_2, 0.7% C_2H_4, and 0.05% C_2H_6. Incomplete decomposition of the CH_4

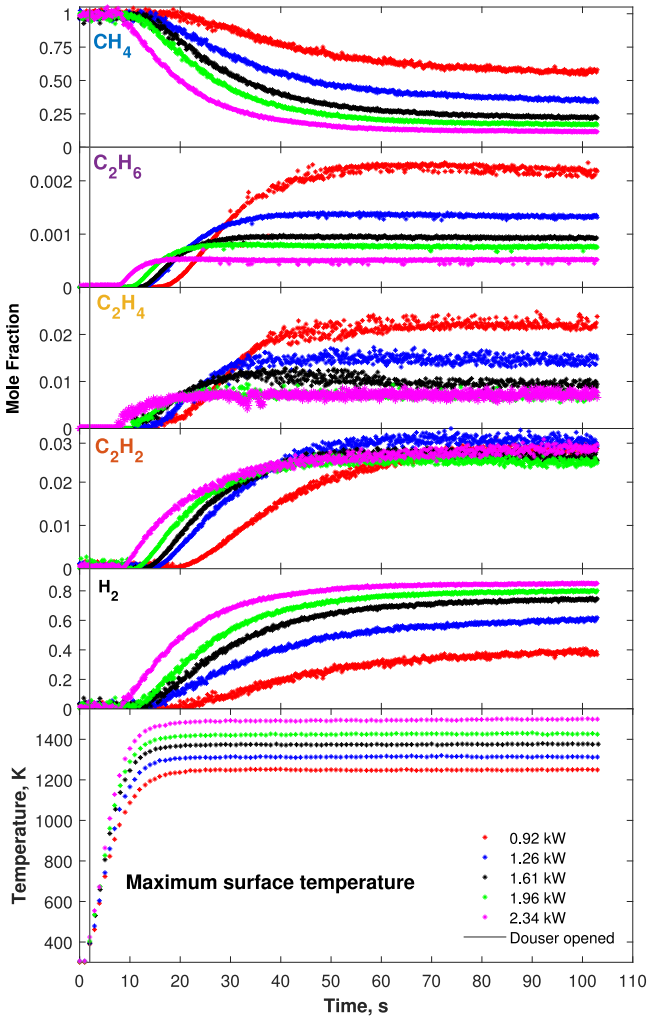

Fig. 11. (Top) Transient mole fraction measurements of CH_4, C_2H_6, C_2H_4, and C_2H_2 and calculated mole fractions of H_2 across a range of lamp output powers. (Bottom) Maximum rear surface temperature of the carbon substrate.

feed gas is partially attributed to the non-uniform temperature distribution of the reaction zone. This non-uniform temperature distribution, with large variations in temperature between the hot and cold regions of the porous substrate gives rise to a spatially-inhomogeneous decomposition reaction. Regions at higher temperatures facilitate greater progression of the decomposition along the dehydrogenation pathway. In contrast, colder regions inhibit complete decomposition of CH_4, with these temperatures yielding greater quantities of the lower C:H intermediate species. Regions on the periphery of the substrate with surface temperatures around 700 K likely prevent any decomposition of CH_4 at all, allowing the inlet CH_4 gas to flow through unreacted. It should be noted that the magnitudes of the minor hydrocarbons are generally higher than that predicted by chemical equilibrium, suggesting that the reacting flow is getting kinetically frozen along the reaction path where higher mole fractions are observed (see Fig. 1).

The measured species evolutions at the start-up of the reactor are similarly consistent with the dehydrogenation kinetic pathway defined in Eq. (2). This stepwise dehydrogenation of CH_4 is captured in the relative durations taken by the minor species to reach steady-state. The measurements show the first minor hydrocarbon in the reaction pathway, C_2H_6, reaches steady-state the earliest followed by C_2H_4 and finally C_2H_2, in increasing order of C:H ratio. The time taken to reach steady-state for C_2H_6 and C_2H_4 are similar, likely due to C_2H_6 being relatively unstable at these reaction temperatures and decomposing quickly to form C_2H_4. This behavior is more pronounced at the lower power input (such as the 0.92 kW case) reflective of the slower kinetics and longer timescales generally. The trends are also corroborated through kinetic simulations of CH_4 decomposition in CANTERA, as shown in Fig. 1.

The measurement precision (or 1σ detection limit) of the sensor in the solar reactor environment is estimated by calculating the minimum resolvable absorbance for each species which occurred during the transient measurements. The measurement resolution is estimated to be 0.2% for CH_4, 700 ppm for C_2H_2, 600 ppm for C_2H_4, and 30 ppm for C_2H_6 at an optical pathlength of 8.2 cm, pressure of 25 torr, and temperature of 298 K. The relative uncertainty for all species lies in the 3%–13% range primarily due to uncertainties in the spectroscopic reference parameters and the conditions of the reactor. These uncertainties are limited by noise/precision limits at the early formation times for acetylene, ethylene, and ethane but for most of the test duration and always for methane, the SNR was greater than 10. The measurement resolution of H_2 is inferred to be approximately 0.3%, and the estimated uncertainty in inferred X_{H_2} is ~4%, obtained by summing the measurement uncertainties of each hydrocarbon in quadrature whilst also accounting for their relative proportions in the product stream at a typical operating condition. Given the indirect quantification of H_2 yield and the relative abundance of CH_4 in the product stream, this resolution value is heavily dominated by the resolution and uncertainty of the CH_4 measurement. Further details on uncertainty calculations may be found in the appendix.

5. Conclusion

In this work, a mid-infrared laser absorption sensor was developed for simultaneous time-resolved species measurements of the four most abundant hydrocarbons (CH_4, C_2H_2, C_2H_4, and C_2H_6) in the pyrolysis of natural gas or methane, providing for a measurement of hydrogen yield through molar balance. The fundamental C-H stretch vibrational bands in the 3.00–3.34 μm wavelength range were exploited to probe multiple strongly absorbing transitions of these hydrocarbons. A time-division multiplexed technique combined with correction methods to remove cross-species spectral interference was employed to successfully obtain mole fraction measurements of the four species at a repetition rate of 10 kHz.

In addition, two neighboring C_2H_2 transitions were leveraged for the application of a two-line thermometry technique that yielded accurate inference of gas temperature up to 805 K. The thermodynamic range of the sensor was further validated across a range of temperatures and pressures on a high-temperature gas cell using mixture compositions relevant to the decomposition of natural gas and methane at sub-atmospheric pressures. While acetylene and methane exhibited good detectability up to 800–1000 K, ethylene and ethane detectability was limited to lower temperatures (~600 K), with limitations associated with the inverse temperature dependence of differential absorbance, spectral database inadequacies, and convolution by spectral interference from methane. A database of methane cross-sections in the 2996.7 cm^{-1}–2997.5 cm^{-1} range was built for interference mitigation of the ethane measurement and is included in the supplementary material up to a temperature of 805 K.

The multi-species sensing capability was demonstrated for in situ analysis in a solar-thermal pyrolysis reactor, where simultaneous time-resolved species measurements elucidated the transient behavior of the reactor at a range of experimentally-simulated insolation conditions. The sub-atmospheric operating envelope of the reactor provided for high-quality measurements of all 4 target species and time-resolved quantification of X_{H_2} through the major products assumption. These measurements demonstrated the utility of the sensor for deployment in hydrocarbon pyrolysis reactors and solar-thermochemical systems, where real-time monitoring of the product stream is critical for robust

process control due to intermittency of insolation throughout a given day. Future work is expected to leverage the expanded operating range of this sensor to perform species measurements further upstream in the solar pyrolysis reactor, near the heterogeneous reaction zone, to further understand the chemical physics involved.

Declaration of competing interest

The authors declare the following financial interests/personal relationships which may be considered as potential competing interests: TSF and RMS are co-founders of a company (SolGraph Inc.) that is involved with solar-thermal material synthesis. The submitted work is an academic study outside the scope of this activity and is not intended or represented as a commercial product or promotion.

Data availability

The methane cross-sections are available as supplementary material to the article. Other data are available upon request.

Acknowledgments

The authors thank A. Alghfeli for his contribution in co-building the simulated solar source and laboratory general instrumentation. The authors also thank N.M. Kuenning and K.K. Schwarm for helpful discussions relating to signal and data processing techniques. This work was supported by the California NanoSystems Institute at UCLA and its Noble Family Innovation Fund as well as the California Energy Commission (PIR-21-004).

Appendix A. Product gas transit time

The transit time of the product gas from the heterogeneous reaction zone to the LAS measurement location was calculated using the equation below:

$$\tau = \frac{L\rho A}{\dot{m}} \tag{A.1}$$

Here, L is the total distance traveled by the gas, ρ is the density of the gas (assumed to be pure CH_4 at the start of decomposition), A is the cross-sectional area of the flow, and $\dot{m}$ is the mass flow rate of the gas. In the evaluation of the transit time, the non-uniform cross-sectional areas of the reaction chamber and the exhaust tube were considered separately when evaluating Eq. (A.1). The individual results were then summed to obtain a final representative value. Given the transient nature of the process, an aggregate gas temperature of 800 K was assumed in the reaction chamber and 300 K in the exhaust tube to approximate ρ.

Appendix B. Uncertainty analysis

The Taylor series method (TSM) of uncertainty propagation [23] was applied with reference to Eq. (4) to calculate the relative uncertainties in the measured mole fractions as follows:

$$\frac{\Delta X_{\text{abs}}}{X_{\text{abs}}} = \sqrt{\left(\frac{\Delta\alpha_v}{\alpha_v}\right)^2 + \left(\frac{\Delta P}{P}\right)^2 + \left(\frac{\Delta S_i(T)}{S_i(T)}\right)^2} \tag{B.1}$$

Here, a 0.5% uncertainty is used for the pressure measurement and linestrength uncertainties are obtained from the respective spectroscopic databases. The uncertainty in temperature at the measurement conditions of the reactor (near room temperature) is minor and is thus excluded from Eq. (B.1). Applying Eq. (B.1) at a representative condition during the decomposition of CH_4 at the highest lamp output power (2.34 kW) yielded species uncertainties of 2.5% in CH_4, 4% in C_2H_2, 11% in C_2H_4, and 3% in C_2H_6, respectively.

$$\Delta X_{H_2} = \sqrt{\left(\frac{\partial X_{H_2}}{\partial X_{CH_4}}\Delta X_{CH_4}\right)^2 + \left(\frac{\partial X_{H_2}}{\partial X_{C_2H_2}}\Delta X_{C_2H_2}\right)^2 + \left(\frac{\partial X_{H_2}}{\partial X_{C_2H_4}}\Delta X_{C_2H_4}\right)^2 + \left(\frac{\partial X_{H_2}}{\partial X_{C_2H_6}}\Delta X_{C_2H_6}\right)^2} \tag{B.2}$$

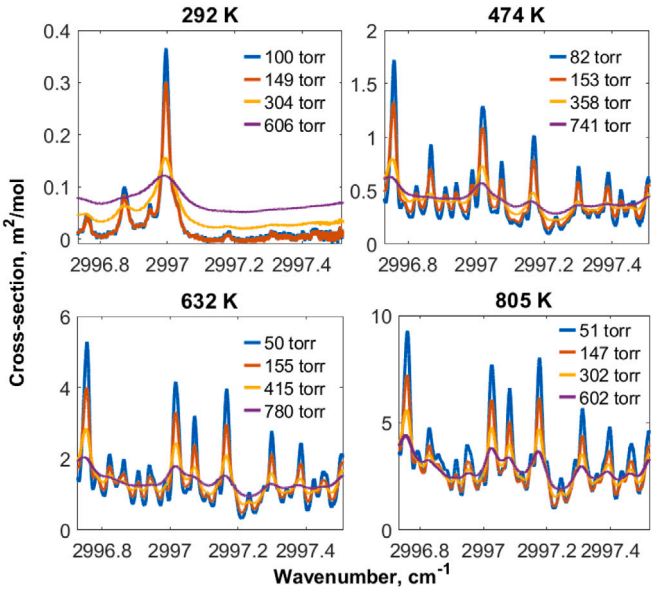

Fig. C.12. Select CH_4 cross-sections across a range of temperatures and pressures. The cross-sections given at each temperature and pressure represent an average of the cross-sections collected for a single test.

Appendix C. Supplementary data

The supplementary material consists of four absorption cross-section files: `CH4_cross_sec_292K.csv`, `CH4_cross_sec_474K.csv`, `CH4_cross_sec_632K.csv`, and `CH4_cross_sec_805K.csv` are comma-separated values files of the measured CH_4 cross-sections in the 2996.7 cm^{-1}–2997.5 cm^{-1} range at 292 K, 474 K, 632 K, and 805 K respectively. The pressures are varied from 50 to 780 torr to include spectra dominated by Doppler and pressure broadening. All the measurements are performed in pure CH_4. The first row of these files contains the pressures at which each cross-section measurement was made, in *torr*. The second row and first column constitute the wavenumber and each subsequent column is the cross-section at each pressure, in mol/m^2. These cross-sections are represented in Fig. C.12.

Supplementary material related to this article can be found online at https://doi.org/10.1016/j.jaecs.2023.100223.

References

[1] Edwards P, Kuznetsov V, David W, Brandon N. Hydrogen and fuel cells: Towards a sustainable energy future. Energy Policy 2008;36(12):4356–62. http://dx.doi.org/10.1016/j.enpol.2008.09.036.

[2] Nikolaidis P, Poullikkas A. A comparative overview of hydrogen production processes. Renew Sustain Energy Rev 2017;67:597–611. http://dx.doi.org/10.1016/j.rser.2016.09.044.

[3] Pudukudy M, Yaakob Z, Takriff MS. Methane decomposition over pd promoted Ni/MgAl 2 O 4 catalysts for the production of COx free hydrogen and multiwalled carbon nanotubes. Appl Surf Sci 2015;356:1320–6. http://dx.doi.org/10.1016/j.apsusc.2015.08.246.

[4] Kothari R, Buddhi D, Sawhney R. Comparison of environmental and economic aspects of various hydrogen production methods. Renew Sustain Energy Rev 2008;12(2):553–63. http://dx.doi.org/10.1016/j.rser.2006.07.012.

[5] Alves L, Pereira V, Lagarteira T, Mendes A. Catalytic methane decomposition to boost the energy transition: Scientific and technological advancements. Renew Sustain Energy Rev 2021;137:110465. http://dx.doi.org/10.1016/j.rser.2020.110465.

[6] Qian JX, Chen TW, Enakonda LR, Liu DB, Mignani G, Basset J-M, et al. Methane decomposition to produce CO -free hydrogen and nano-carbon over metal catalysts: A review. Int J Hydrogen Energy 2020;45(15):7981–8001. http://dx.doi.org/10.1016/j.ijhydene.2020.01.052.

[7] Rodat S, Abanades S, Flamant G. Co-production of hydrogen and carbon black from solar thermal methane splitting in a tubular reactor prototype. Sol Energy 2011;85(4):645–52. http://dx.doi.org/10.1016/j.solener.2010.02.016.

[8] Wang H, You X, Joshi AV, Davis SG, Laskin A, Egolfopoulos F, et al. USC Mech Version II. High-temperature combustion reaction model of H2/CO/C1-C4 Compounds. 2007, http://ignis.usc.edu/USC_Mech_II.htm.
[9] Yao S, Weng S, Jin Q, Lu H, Wu Z, Zhang X, et al. Mechanism of decane decomposition in a pulsed dielectric barrier discharge reactor. IEEE Trans Plasma Sci 2016;44(11):2660–6. http://dx.doi.org/10.1109/tps.2016.2573641.
[10] Tezel E, Figen HE, Baykara SZ. Hydrogen production by methane decomposition using bimetallic Ni–Fe catalysts. Int J Hydrogen Energy 2019;44(20):9930–40. http://dx.doi.org/10.1016/j.ijhydene.2018.12.151.
[11] Torres D, de Llobet S, Pinilla J, Lázaro M, Suelves I, Moliner R. Hydrogen production by catalytic decomposition of methane using a fe-based catalyst in a fluidized bed reactor. J Nat Gas Chem 2012;21(4):367–73. http://dx.doi.org/10.1016/s1003-9953(11)60378-2.
[12] Moshrefi MM, Rashidi F. Hydrogen production from methane decomposition in cold plasma reactor with rotating electrodes. Plasma Chem Plasma Process 2018;38(3):503–15. http://dx.doi.org/10.1007/s11090-018-9875-5.
[13] Abanades S, Kimura H, Otsuka H. Hydrogen production from thermo-catalytic decomposition of methane using carbon black catalysts in an indirectly-irradiated tubular packed-bed solar reactor. Int J Hydrogen Energy 2014;39(33):18770–83. http://dx.doi.org/10.1016/j.ijhydene.2014.09.058.
[14] Gao X, Fan H, Huang T, Wang X, Bao J, Li X, et al. Natural gas pipeline leak detector based on NIR diode laser absorption spectroscopy. Spectrochim Acta A 2006;65(1):133–8. http://dx.doi.org/10.1016/j.saa.2005.09.046.
[15] Xi Z, Zheng K, Zheng C, Zhang H, Song F, Li C, et al. Near-infrared dual-gas sensor system for methane and ethane detection using a compact multipass cell. Front Phys 2022;10. http://dx.doi.org/10.3389/fphy.2022.843171.
[16] Stranic I, Hanson RK. Laser absorption diagnostic for measuring acetylene concentrations in shock tubes. J Quant Spectrosc Radiat Transfer 2014;142:58–65. http://dx.doi.org/10.1016/j.jqsrt.2014.03.024.
[17] Ren W, Davidson DF, Hanson RK. IR laser absorption diagnostic for C2H4 in shock tube kinetics studies. Int J Chem Kinet 2012;44(6):423–32. http://dx.doi.org/10.1002/kin.20599.
[18] Cassady SJ, Choudhary R, Pinkowski NH, Shao J, Davidson DF, Hanson RK. The thermal decomposition of ethane. Fuel 2020;268:117409. http://dx.doi.org/10.1016/j.fuel.2020.117409.
[19] Webster CR. Measuring methane and its isotopes $^{12}CH_4$, $^{13}CH_4$, and CH_3D on the surface of Mars with in situ laser spectroscopy. Appl Opt 2005;44(7):1226. http://dx.doi.org/10.1364/ao.44.001226.
[20] Li J, Nair AP, Schwarm KK, Pineda DI, Spearrin RM. Temperature-dependent line mixing in the R-branch of the v3 band of methane. J Quant Spectrosc Radiat Transfer 2020;255:107271. http://dx.doi.org/10.1016/j.jqsrt.2020.107271.
[21] Sun J, Chang J, Zhang Y, Wei Y, Zhang Q, Wang F, et al. CH4/C2H6 dual gas sensing system using a single mid-infrared laser. Spectrochim Acta A 2023;291:122368. http://dx.doi.org/10.1016/j.saa.2023.122368.
[22] Goodwin DG, Moffat HK, Speth RL. Cantera: An object-oriented software toolkit for chemical kinetics, thermodynamics, and transport processes. Version 2.3.0. Zenodo; 2017, http://dx.doi.org/10.5281/ZENODO.170284.
[23] Wei C, Abuseada M, Jeevaretanam B, Fisher TS, Spearrin RM. Concentrated solar-thermal methane pyrolysis in a porous substrate: Yield analysis via infrared laser absorption. Proc Combust Inst 2023;39(4):5581–9. http://dx.doi.org/10.1016/j.proci.2022.07.007.
[24] Hanson RK, Spearrin RM, Goldenstein CS. Spectroscopy and optical diagnostics for gases. Springer International Publishing; 2016, http://dx.doi.org/10.1007/978-3-319-23252-2.
[25] Wei C, Schwarm KK, Pineda DI, Spearrin RM. Deep neural network inversion for 3D laser absorption imaging of methane in reacting flows. Opt Lett 2020;45(8):2447. http://dx.doi.org/10.1364/ol.391834.
[26] Mandin J-Y, Jacquemart D, Dana V, Régalia-Jarlot L, Barbe A. Line intensities of acetylene at. J Quant Spectrosc Radiat Transfer 2005;92(2):239–60. http://dx.doi.org/10.1016/j.jqsrt.2004.07.024.
[27] Schwarm KK, Wei C, Pineda DI, Spearrin RM. Time-resolved laser absorption imaging of ethane at 2 kHz in unsteady partially premixed flames. Appl Opt 2019;58(21):5656. http://dx.doi.org/10.1364/ao.58.005656.
[28] Hargreaves RJ, Gordon IE, Rey M, Nikitin AV, Tyuterev VG, Kochanov RV, et al. An accurate, extensive, and practical line list of methane for the HITEMP database. Astrophys J Suppl Ser 2020;247(2):55. http://dx.doi.org/10.3847/1538-4365/ab7a1a.
[29] Gordon I, Rothman L, Hargreaves R, Hashemi R, Karlovets E, Skinner F, et al. The HITRAN2020 molecular spectroscopic database. J Quant Spectrosc Radiat Transfer 2022;277:107949. http://dx.doi.org/10.1016/j.jqsrt.2021.107949.
[30] Harrison JJ, Allen ND, Bernath PF. Infrared absorption cross sections for ethane (C2H6) in the 3μm region. J Quant Spectrosc Radiat Transfer 2010;111(3):357–63. http://dx.doi.org/10.1016/j.jqsrt.2009.09.010.
[31] Nair AP, Minesi NQ, Jelloian C, Kuenning NM, Spearrin RM. Extended tuning of distributed-feedback lasers in a bias-tee circuit via waveform optimization for MHz-rate absorption spectroscopy. Meas Sci Technol 2022;33(10):105104. http://dx.doi.org/10.1088/1361-6501/ac7b13.
[32] Schwarm KK, Dinh HQ, Goldenstein CS, Pineda DI, Spearrin RM. High-pressure and high-temperature gas cell for absorption spectroscopy studies at wavelengths up to 8 μm. J Quant Spectrosc Radiat Transfer 2019;227:145–51. http://dx.doi.org/10.1016/j.jqsrt.2019.01.029.
[33] Wei C, Pineda DI, Paxton L, Egolfopoulos FN, Spearrin RM. Mid-infrared laser absorption tomography for quantitative 2D thermochemistry measurements in premixed jet flames. Appl Phys B 2018;124(6). http://dx.doi.org/10.1007/s00340-018-6984-z.
[34] Abuseada M, Wei C, Spearrin RM, Fisher TS. Solar–thermal production of graphitic carbon and hydrogen via methane decomposition. Energy Fuels 2022;36(7):3920–8. http://dx.doi.org/10.1021/acs.energyfuels.1c04405.
[35] Abuseada M, Alghfeli A, Fisher TS. Indirect inverse flux mapping of a concentrated solar source using infrared imaging. Rev Sci Instrum 2022;93(7). http://dx.doi.org/10.1063/5.0090855.
[36] Abuseada M, Ophoff C, Ozalp N. Characterization of a new 10 kWe high flux solar simulator via indirect radiation mapping technique. J Solar Energy Eng 2019;141(2). http://dx.doi.org/10.1115/1.4042246.
[37] Abuseada M, Ozalp N. Experimental and numerical study on heat transfer driven dynamics and control of transient variations in a solar receiver. Sol Energy 2020;211:700–11. http://dx.doi.org/10.1016/j.solener.2020.10.009.
[38] Davidson DF, Hanson RK, Bowman CT. Revised values for the rate coefficients of ethane and methane decomposition. Int J Chem Kinet 1995;27(3):305–8. http://dx.doi.org/10.1002/kin.550270308.